

# Tight control of light beams in photonic crystals with spatially-variant lattice orientation

Jennifer L. Digaum,<sup>1</sup> Javier J. Pazos,<sup>2</sup> Jeffrey Chiles,<sup>1</sup> Jeffrey D' Archangel,<sup>1</sup>  
Gabriel Padilla,<sup>3</sup> Adrian Tatulian,<sup>4</sup> Raymond C. Rumpf,<sup>2</sup> Sasan Fathpour,<sup>1,5</sup>  
Glenn D. Boreman,<sup>6</sup> and Stephen M. Kuebler,<sup>1,3,4,\*</sup>

<sup>1</sup>CREOL, The College of Optics & Photonics, University of Central Florida, Orlando, Florida 32816, USA

<sup>2</sup>EM Lab, W. M. Keck Center for 3D Innovation, University of Texas at El Paso, El Paso, Texas 79968, USA

<sup>3</sup>Chemistry Department, University of Central Florida, Orlando, Florida 32816, USA

<sup>4</sup>Physics Department, University of Central Florida, Orlando, Florida 32816, USA

<sup>5</sup>Department of Electrical Engineering & Computer Science, University of Central Florida, Orlando, Florida 32816, USA

<sup>6</sup>Department of Physics and Optical Science, University of North Carolina at Charlotte, Charlotte, North Carolina 28223, USA

\*kuebler@ucf.edu

**Abstract:** Spatially-variant photonic crystals (SVPCs), in which the orientation of the unit cell changes as a function of position, are shown to be capable of abruptly controlling light beams using just low index materials and can be made to have high polarization selectivity. Multi-photon direct laser writing in the photo-polymer SU-8 was used to fabricate three-dimensional SVPCs that direct the flow of light around a 90 degree bend. The lattice spacing and fill factor were maintained nearly constant throughout the structure. The SVPCs were characterized at a wavelength of 2.94  $\mu\text{m}$  by scanning the faces with optical fibers and the results were compared to electromagnetic simulations. The lattices were shown to direct infrared light of one polarization through sharp bends while the other polarization propagated straight through the SVPC. This work introduces a new scheme for controlling light that should be useful for integrated photonics.

©2014 Optical Society of America

**OCIS codes:** (350.4238) Nanophotonics and photonic crystals; (160.3918) Metamaterials; (160.5293) Photonic bandgap materials; (220.4000) Microstructure fabrication; (350.3390) Laser materials processing.

---

## References and links

1. E. A. J. Marcatili, "Bends in optical dielectric guides," *Bell Syst. Tech. J.* **48**(7), 2103–2132 (1969).
2. J. Witzens, M. Lončar, and A. Scherer, "Self-collimation in planar photonic crystals," *IEEE J. Sel. Top. Quant.* **8**(6), 1246–1257 (2002).
3. R. Iliew, C. Etrich, and F. Lederer, "Self-collimation of light in three-dimensional photonic crystals," *Opt. Express* **13**(18), 7076–7085 (2005).
4. R. C. Rumpf, J. Pazos, C. R. Garcia, L. Ochoa, and R. Wicker, "3D printed lattices with spatially variant self-collimation," *Prog. Electromagnetics Res.* **139**, 1–14 (2013).
5. O. Vanbésien and E. Centeno, *Dispersion Engineering for Integrated Nanophotonics* (ISTE Ltd., 2014).
6. K. V. Do, X. Le Roux, D. Marris-Morini, L. Vivien, and E. Cassan, "Experimental demonstration of light bending at optical frequencies using a non-homogenizable graded photonic crystal," *Opt. Express* **20**(4), 4776–4783 (2012).
7. O. Miță, C.-G. Bostan, and P. Şchiopu, "Structureless interconnects for photonic integrated circuits," *U. Politeh. Buch. Ser. A* **76**(1), 205–214 (2014).
8. D. W. Prather, S. Y. Shi, J. Murakowski, G. J. Schneider, A. Sharkawy, C. H. Chen, B. L. Miao, and R. Martin, "Self-collimation in photonic crystal structures: a new paradigm for applications and device development," *J. Phys. D Appl. Phys.* **40**(9), 2635–2651 (2007).
9. E. Akmansoy, E. Centeno, K. Vynck, D. Cassagne, and J. M. Lourtioz, "Graded photonic crystals curve the flow of light: An experimental demonstration by the mirage effect," *Appl. Phys. Lett.* **92**(13), 133501 (2008).
10. E. Cassan, K. V. Do, C. Caer, D. Marris-Morini, and L. Vivien, "Short-wavelength light propagation in graded photonic crystals," *J. Lightwave Technol.* **29**(13), 1937–1943 (2011).

11. E. Centeno and D. Cassagne, "Graded photonic crystals," *Opt. Lett.* **30**(17), 2278–2280 (2005).
12. Y. Y. Li, M. Y. Li, P. F. Gu, Z. R. Zheng, and X. Liu, "Graded wavelike two-dimensional photonic crystal made of thin films," *Appl. Opt.* **47**(13), C70–C74 (2008).
13. L. H. Gabrielli and M. Lipson, "Integrated Luneburg lens via ultra-strong index gradient on silicon," *Opt. Express* **19**(21), 20122–20127 (2011).
14. D. H. Spadoti, L. H. Gabrielli, C. B. Poitras, and M. Lipson, "Focusing light in a curved-space," *Opt. Express* **18**(3), 3181–3186 (2010).
15. B. Vasić, G. Isić, R. Gajić, and K. Hingerl, "Controlling electromagnetic fields with graded photonic crystals in metamaterial regime," *Opt. Express* **18**(19), 20321–20333 (2010).
16. S. Hayashi and T. Okamoto, "Plasmonics: visit the past to know the future," *J. Phys. D Appl. Phys.* **45**(43), 433001 (2012).
17. M. L. Brongersma and P. G. Kik, eds., *Surface Plasmon Nanophotonics*, Springer Series in Optical Sciences (Springer Verlag, 2007), Vol. 131.
18. K. L. Tsakmakidis and O. Hess, "Extreme control of light in metamaterials: Complete and loss-free stopping of light," *Physica B* **407**(20), 4066–4069 (2012).
19. O. Hess, J. B. Pendry, S. A. Maier, R. F. Oulton, J. M. Hamm, and K. L. Tsakmakidis, "Active nanoplasmonic metamaterials," *Nat. Mater.* **11**(7), 573–584 (2012).
20. W. S. Cai, W. Shin, S. H. Fan, and M. L. Brongersma, "Elements for plasmonic nanocircuits with three-dimensional slot waveguides," *Adv. Mater.* **22**(45), 5120–5124 (2010).
21. W. Shin, W. S. Cai, P. B. Catrysse, G. Veronis, M. L. Brongersma, and S. H. Fan, "Broadband sharp 90-degree bends and T-splitters in plasmonic coaxial waveguides," *Nano Lett.* **13**(10), 4753–4758 (2013).
22. D. F. Pile and D. K. Gramotnev, "Plasmonic subwavelength waveguides: next to zero losses at sharp bends," *Opt. Lett.* **30**(10), 1186–1188 (2005).
23. H. Chen, C. T. Chan, and P. Sheng, "Transformation optics and metamaterials," *Nat. Mater.* **9**(5), 387–396 (2010).
24. D.-H. Kwon and D. H. Werner, "Transformation Electromagnetics: an overview of the theory and applications," *IEEE Trans. Antenn. Propag.* **52**(1), 24–46 (2010).
25. D.-H. Kwon and D. H. Werner, "Transformation optical designs for wave collimators, flat lenses and right-angle bends," *New J. Phys.* **10**(11), 115023 (2008).
26. Y. Liu and X. Zhang, "Recent advances in transformation optics," *Nanoscale* **4**(17), 5277–5292 (2012).
27. H. E. Williams, Z. Luo, and S. M. Kuebler, "Effect of refractive index mismatch on multi-photon direct laser writing," *Opt. Express* **20**(22), 25030–25040 (2012).
28. R. C. Rumpf and J. Pazos, "Synthesis of spatially variant lattices," *Opt. Express* **20**(14), 15263–15274 (2012).
29. S. Keller, G. Blagoi, M. Lillemose, D. Haefliger, and A. Boisen, "Processing of thin SU-8 films," *J. Micromech. Microeng.* **18**(12), 125020 (2008).
30. R. C. Rumpf and J. J. Pazos, "Optimization of planar self-collimating photonic crystals," *J. Opt. Soc. Am. A* **30**(7), 1297–1304 (2013).
31. S. M. Kuebler and M. Rumi, "Nonlinear optics—applications: three-dimensional microfabrication," in *Encyclopedia of Modern Optics*, R. D. Guenther, D. G. Steel, and L. Bayvel, eds. (Elsevier, 2004), pp. 189–206.
32. R. C. Rumpf, "Simple implementation of arbitrarily shaped total-field/scattered-field regions in finite-difference frequency-domain," *Prog. Electromagnetics Res.* **36**, 221–248 (2012).
33. D. J. Dikken, M. Spasenović, E. Verhagen, D. van Oosten, and L. K. Kuipers, "Characterization of bending losses for curved plasmonic nanowire waveguides," *Opt. Express* **18**(15), 16112–16119 (2010).
34. Q. Wang, G. Farrell, P. F. Wang, G. Rajan, and T. Freir, "Design of integrated wavelength monitor based on a Y-branch with an S-bend waveguide," *Sens. Actuator A-Phys.* **134**(2), 405–409 (2007).
35. R. Wollhofen, J. Katzmann, C. Hrelescu, J. Jacak, and T. A. Klar, "120 nm resolution and 55 nm structure size in STED-lithography," *Opt. Express* **21**(9), 10831–10840 (2013).
36. L. J. Li, R. R. Gattass, E. Gershgoren, H. Hwang, and J. T. Fourkas, "Achieving  $\lambda/20$  resolution by one-color initiation and deactivation of polymerization," *Science* **324**(5929), 910–913 (2009).
37. T. Bückmann, N. Stenger, M. Kadic, J. Kaschke, A. Frölich, T. Kennerknecht, C. Eberl, M. Thiel, and M. Wegener, "Tailored 3D mechanical metamaterials made by dip-in direct-laser-writing optical lithography," *Adv. Mater.* **24**(20), 2710–2714 (2012).
38. B. B. Oner, M. Turduev, and H. Kurt, "High-efficiency beam bending using graded photonic crystals," *Opt. Lett.* **38**(10), 1688–1690 (2013).
39. D. Gao, Z. Zhou, and D. S. Citrin, "Self-collimated waveguide bends and partial bandgap reflection of photonic crystals with parallelogram lattice," *J. Opt. Soc. Am. A* **25**(3), 791–795 (2008).
40. L. H. Gabrielli, D. Liu, S. G. Johnson, and M. Lipson, "On-chip transformation optics for multimode waveguide bends," *Nat Commun* **3**, 1217, 1217–6 (2012).
41. M. Shur, "Terahertz technology: devices and applications," *Proceedings of the 35th European Solid-State Device Research Conference (Grenoble, France, 2005)*, pp. 13–25.

## 1. Introduction

Integrated photonic systems require abrupt control of optical beams for routing light signals, controlling polarization, and more. Ideally, this would be accomplished using simple optical

structures made from ordinary materials. Waveguides based on total internal reflection require turn radii that are hundreds to thousands of times larger than the vacuum wavelength  $\lambda_0$ , depending upon the refractive index contrast, to ensure negligible bending loss due to mode leakage [1]. Furthermore, the beam must conform to the mode shape of the waveguide to be controlled. These considerations limit the extent to which waveguides can be used for integrated photonics.

Here we show that ultracompact control of optical beams can be accomplished using self-collimating three-dimensional (3D) spatially-variant photonic crystals (SVPCs), by demonstrating that an unguided beam can be made to flow around a  $90^\circ$  bend with a radius  $R_{\text{bend}}$  as small as  $6.4\lambda_0$ , as in Fig. 1. Self-collimation is an effect in photonic crystals where beams are forced to propagate along an axis of the lattice, without diffraction [2,3]. Beams can be made to flow along arbitrary paths by “bending” the lattice, as long as the size and shape of the unit cells can be held constant [4]. The self-collimation effect is resilient to absorption loss and can provide abrupt control of optical beams using low refractive index materials. In contrast to waveguides that confine beams to a specific area, self-collimation can occur in any part of the lattice and can even be used to manipulate wave fronts and images.

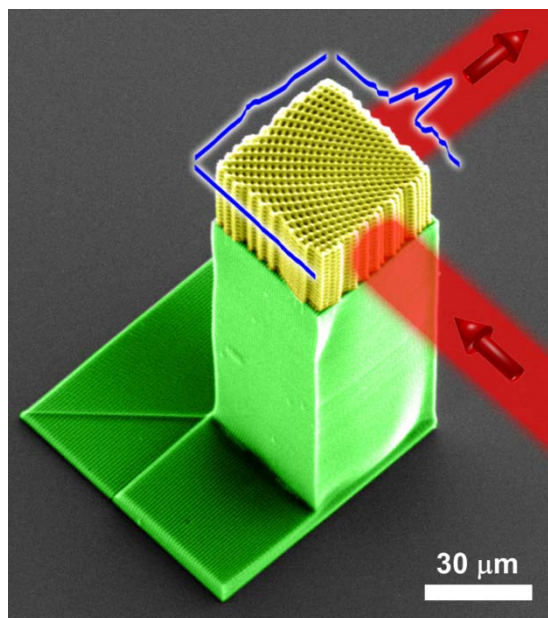


Fig. 1. False-color scanning electron microscopy (SEM) image of a spatially-variant photonic crystal (SVPC, depicted in yellow) having a fill factor of 53%, for which the orientation of adjacent unit cells is progressively rotated to direct the flow of light through a  $90^\circ$  turn (red). The SVPC is supported above the substrate by a pedestal (green). The blue ribbons are the experimentally measured relative intensity exiting each face of the SVPC when an optic fiber introduced light having  $\lambda_0 = 2.94 \mu\text{m}$  onto the lattice. The data show that light was directed through a turn with radius  $R_{\text{bend}} = 6.4\lambda_0$ . The SVPC was fabricated by multi-photon direct laser writing (DLW) in SU-8, a cross-linkable epoxide.

In photonic crystals, light propagates in a direction that is normal to the dispersion surface, which is a visual representation in  $k$ -space of the supported eigenmodes. A cross-section of the dispersion surface yields isofrequency contours (IFCs) which describe the spatial dispersion of the lattice at a given frequency [5]. A flat IFC corresponds to a frequency and  $k$ -space over which light propagates with little or no divergence, and this effect has been called “self-collimation” [2,3]. It should be noted that this is a purely passive optical effect that does not require active or nonlinear processes, like self-focusing. Self-collimation has

been proposed as a means for guiding waves in integrated photonic circuits [6–8], but no mechanism for flowing beams along arbitrary paths was suggested.

Alternative techniques for bending unguided beams include graded photonic crystals [6,9–12] and graded-index materials [13–15]. At a macroscopic level these produce bending through refraction, whereas SVPCs utilize diffraction. Graded photonic crystals exploit the dispersion near a band edge to tune the effective refractive index. Graded-index materials derive their performance from spatially slow variation of the average material properties. The main disadvantage of these two approaches is that neither can bend a beam as abruptly as SVPCs without using very high refractive index materials, or metals, which introduce ohmic loss [16]. Additionally, both require that composition, structure, or fill factor of a unit cell is varied to control the effective index throughout the lattice to refract a beam around a bend. This substantially increases the complexity of fabrication. Plasmonics [17], metamaterials [18], and their combination [19] also offer means for tight beam control [20–22]. But these schemes also rely upon metallic sub-wavelength structures that require complex fabrication procedures and introduce substantial loss [23]. Transformation optics (TO) is an approach for designing materials and devices in which the permittivity and/or permeability are spatially modified to control the electromagnetic field [24], including bending beams very abruptly [24,25]. While conceptually attractive, designs obtained via TO can be impractical because exotic and typically lossy media are needed, like plasmonic or sub-wavelength metamaterials, to achieve the specific electric and magnetic response [26].

Controlling electromagnetic radiation using SVPCs is a powerful alternative that solves many of the problems associated with the approaches listed above. SVPCs enable beams to be controlled very abruptly using low-index, all-dielectric materials. This eliminates the need for exotic media that are often required for designs obtained via TO, making fabrication easier and reducing losses. Additionally, the feature sizes are larger than those required for metamaterials, again making SVPCs easier to fabricate. SVPCs have been successfully demonstrated for bending microwave radiation around tight turns [4]. Here we show that optical beams can be controlled in SVPCs where it is the *orientation* of the unit cells that is spatially varied instead of fill factor, composition, or structure. This, however, must be done in a way that minimizes deformations to the size and shape of the unit cells, as this would detune or eliminate the self-collimation effect. 3D SVPCs with unit-cell dimensions on the order of two microns were fabricated using multi-photon direct laser writing (DLW) in the photo-polymer SU-8. The SVPCs were optically characterized using light having  $\lambda_0 = 2.94 \mu\text{m}$  and shown to be capable of directing a mid-infrared beam through a turn with  $R_{\text{bend}} = 19 \mu\text{m}$ . To the best of our knowledge, this is the first report demonstrating the use of 3D SVPCs to control optical beams.

## 2. Experimental methods

### 2.1. Preparation of SU-8 films for ellipsometry and fabrication of SVPCs

SU-8 2075 photo-polymer resin (MicroChem) was spin-coated onto standard glass microscope slides for fabrication of SVPCs by DLW. The material was used as received (74 wt-% solids) when preparing thick films ( $> 100 \mu\text{m}$ ), and it was diluted with cyclopentanone (CAS 120-92-3) when preparing thin films. Microscope slides were cut to  $25 \text{ mm} \times 25 \text{ mm}$  sections and cleaned [27]. A  $5 \mu\text{m}$  thick adhesion layer of SU-8 was then applied by spin-coating diluted SU-8 (52 wt-%) onto the substrate (6000 rpm, 30 s), pre-baking the sample on a hotplate ( $65 \text{ }^\circ\text{C}$  for 1 min.;  $95 \text{ }^\circ\text{C}$  for 6 min.), exposing to UV light for 2 min. (Loctite ZETA 7411-5, 400 W metal halide source, 315 - 400 nm), post-baking ( $65 \text{ }^\circ\text{C}$  for 1 min.;  $95 \text{ }^\circ\text{C}$  for 9 min.), and allowing to cool to room temperature. A thick layer of 73.5 wt-% SU-8 was then spin-coated (1400 rpm, 30 s) onto the adhesion-layer-coated substrate, pre-baked ( $65 \text{ }^\circ\text{C}$  for 5 min.;  $95 \text{ }^\circ\text{C}$  for 40 min.), and allowed to cool to room

temperature. This procedure produced a 160  $\mu\text{m}$  film of solid SU-8 that was ready for fabrication of an SVPC by DLW.

### 2.2. Measurement of $n$ and $\kappa$ for SU-8

The complex refractive index  $\tilde{n} = n + i\kappa$  was measured over a span of wavelengths from 500 nm to 10  $\mu\text{m}$  for cured SU-8 by ellipsometry, where  $n$  is the ordinary refractive index and  $\kappa$  is the extinction coefficient. A five inch diameter single-side polished silicon wafer was rinsed with acetone, methanol, and deionized water, and then dried under a stream of nitrogen gas. Diluted SU-8 (29 wt-%) was spin-coated (6000 rpm, 30 s) onto the polished side of the wafer, pre-baked (95  $^{\circ}\text{C}$  for 1 min.), exposed under UV irradiation (1 min.), and post-baked (95  $^{\circ}\text{C}$  for 9 min.). This sample was then used to measure  $n$  and  $\kappa$  by variable-angle spectroscopic ellipsometry (J.A. Woollam VASE and IR-VASE). At  $\lambda_0 = 2.94 \mu\text{m}$ ,  $n = 1.573$ , and  $\kappa = 6.31 \times 10^{-3}$ , which corresponds to an absorption coefficient of  $\alpha = 4\pi\kappa/\lambda_0 = 270 \text{ cm}^{-1}$ . The film thickness was found to be 1.6  $\mu\text{m}$ , and this was independently confirmed by SEM imaging of the sample in cross-section. The profile of  $\kappa$  versus  $\lambda_0$  over the range 1.5  $\mu\text{m}$  to 10  $\mu\text{m}$  was independently verified by transmission Fourier transform infrared spectrophotometry (Jasco 4100 FTIR). A plot of  $n$  and  $\kappa$  versus wavelength is shown in Fig. 2, and the corresponding values are provided in the Appendix.

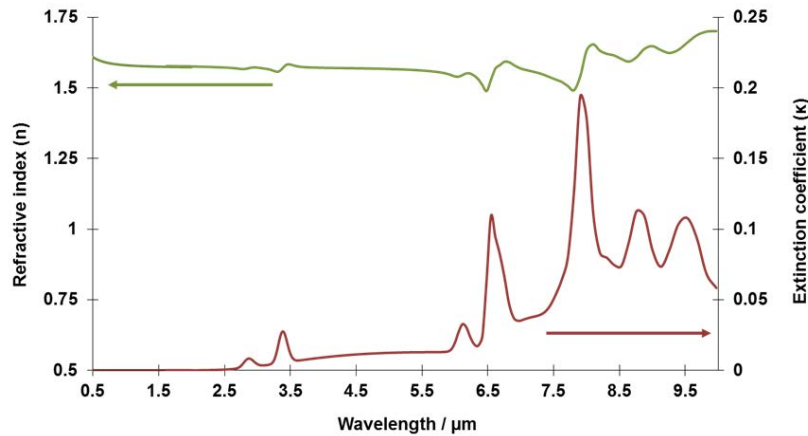


Fig. 2. Plot of refractive index  $n$  and extinction coefficient  $\kappa$  obtained from ellipsometry measurements of a cross-linked 1.6  $\mu\text{m}$  thick SU-8 film using VASE and IR-VASE instruments (J.A. Woollam). The values used to generate this plot are provided in Table 2.

### 2.3. Design of the SVPCs

The design of the SVPCs was based on the process developed by Rumpf *et al.* [28]. Key elements are illustrated in Fig. 3. In single-beam DLW, horizontal scanning of the focal spot produces resolution-limited rods with sub-micron axial and transverse widths typically in the ratio of  $\sim 2.5:1$  [27]. With this in mind, the unit cell was designed to be simple cubic, having edge-length  $a$ , and a basis consisting of three orthogonal intersecting rods with ellipsoidal cross-section, as illustrated in Figs. 3(a) and 3(b). The unit cell resulting from laser exposure was constructed numerically by summing the rods and blurring the resulting pattern using a Gaussian function. The blur operation accounts for acid diffusion that occurs during fabrication [29]. By adding the rods, instead of performing a simple Boolean OR operation, the blurring operation produces greater diffusion where the rods intersect. This is where the corresponding exposure dose and resulting photoacid concentration would be higher, leading to greater diffusion. The blue surface in Figs. 3(a) and 3(b) represents the lattice without accounting for acid diffusion, whereas the red surface shows the more realistic lattice that accounts for acid diffusion after the blur operation. To model the developing process of the

high contrast photopolymer SU-8, a simple threshold was chosen, below which it was assumed that material was dissolved away. This step results in a binary set of data, where “0” represents air and “1” represents cross-linked SU-8. The value of the threshold was chosen to best reproduce the SEM images of the actual structures fabricated by DLW. The threshold was varied to obtain model unit cells with different volumetric fill factor. Using the experimental values of  $n$  and  $\kappa$  obtained from ellipsometry of SU-8, the method of [28] was used to identify values of  $a$  and the fill-factor for unit cells like that shown in Fig. 3 which could be fabricated by single-beam DLW and would be capable of self-collimating at  $\lambda_0 = 2.94 \mu\text{m}$ . At this stage we found that a unit cell having  $a = 2.0 \mu\text{m}$  and a volumetric fill factor near 50% had *nearly* flat isofrequency contours [30] and would be best suited for self-collimation.

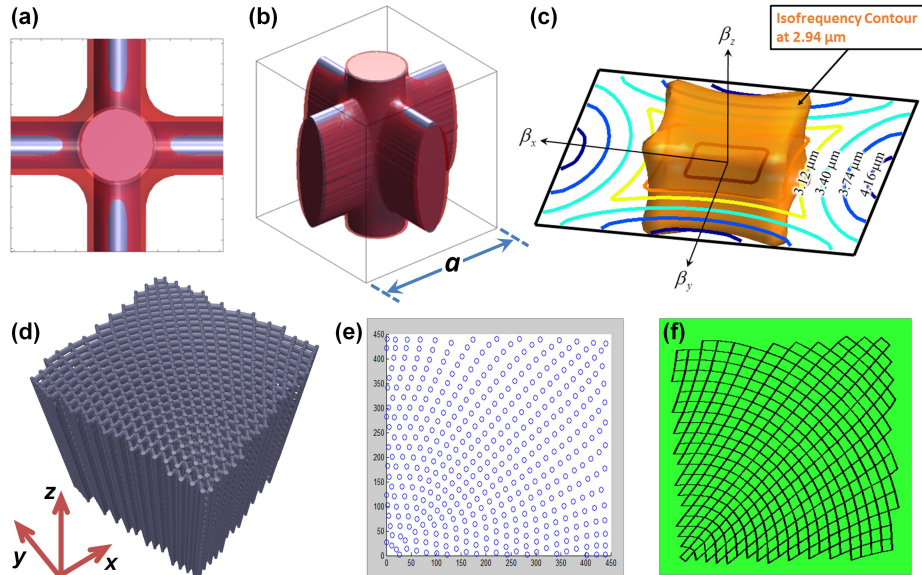


Fig. 3. Illustration of key steps in the process used to design the SVPC lattice. (a) Top- and (b) perspective-views and (c) isofrequency contours of the unit cell produced by modelling DLW exposure and acid diffusion. (d) Perspective view of the SVPC lattice. (e) Centroids of the lattice in one  $xy$ -plane and (f) the corresponding fabrication plan for DLW of the same.

A  $40 \mu\text{m} \times 40 \mu\text{m} \times 40 \mu\text{m}$  SVPC was designed consisting of these unit cells, but with their orientation spatially varied in an azimuthal pattern so that the lattice would direct a beam around a  $90^\circ$  bend [Fig. 3(d)]. The geometry of the lattice was generated using a novel synthesis tool, also developed by Rumpf *et al.* [28], that allows for properties like unit cell orientation, lattice spacing, material composition, fill-factor and others to be spatially varied, while producing a final lattice that is still smooth, continuous, and free of defects. In the present work, only the unit cell orientation was spatially varied. Fluctuations of the other parameters were minimized throughout the lattice, which is critical for maintaining strong self-collimation throughout the bend.

A write-file was generated from the SVPC lattice that defines how the laser beam is scanned within the SU-8 film during DLW. The write-file was created by locating the centroids of the lattice [Fig. 3(e)] and connecting them with line segments that collectively reconstruct the original lattice [Fig. 3(f)]. An additional set of lines was added to the write-file for a solid pedestal in order to elevate the SVPC off the substrate by  $110 \mu\text{m}$ . This ensured that optical fibers could be scanned across the faces without contacting the substrate. The write-file can be scaled to create lattices of different sizes; however, those intended to exhibit

optical function at  $\lambda_0 = 2.94 \mu\text{m}$  were scaled so that unit cells at the center of the SVPC would have  $a = 2.0 \mu\text{m}$ .

#### 2.4. Fabrication of SVPCs by multi-photon direct laser writing in SU-8

The SVPCs were fabricated by DLW in 160  $\mu\text{m}$  thick films of spin-coated SU-8. The method of DLW has been described elsewhere [31] and the specifics of our implementation are reported in [27]. A computer controlled DLW system executed the write-file, translating the sample relative to the focused laser beam at 50  $\mu\text{m}/\text{s}$  with synchronous control of an opto-mechanical shutter to expose along the line-segments that define the pedestal and the SVPC. The average laser power delivered at the sample was varied from 1.8 mW to 2.2 mW to control the cross-sectional dimensions of the resulting polymerized rods. After laser exposure, the sample was post-baked (5 min. at 65  $^\circ\text{C}$  then 15 min. at 95  $^\circ\text{C}$ ), immersed consecutively in two baths of propylene glycol methyl ether acetate (CAS# 108-65-6) for 30 minutes each to remove unexposed resin, rinsed with isopropyl alcohol followed by deionized water, then allowed to dry in air. The free-standing SVPC was inspected by transmission optical microscopy [Fig. 4] to assess its form and quality prior to optical characterization. This process was repeated to fabricate a range of SVPCs each with varying volumetric fill factor. Higher laser powers produced polymerized rods with larger lateral cross section and correspondingly higher volumetric fill factor. To achieve the highest fill factors, rods parallel to the substrate were doubly exposed as pairs of overlapping segments, laterally displaced from the center by 300 nm, to create “super-rods” with larger total cross-section.

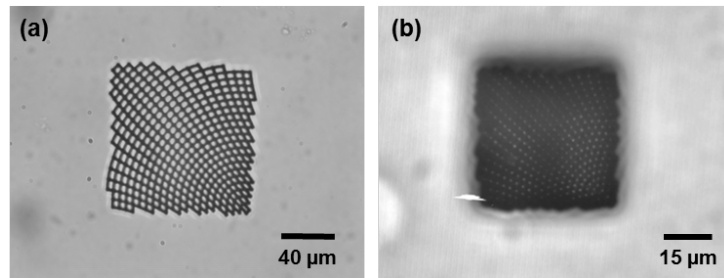


Fig. 4. Optical transmission microscopy images of SVPCs after fabrication by DLW. (a) An SVPC scaled to have  $a = 5.75 \mu\text{m}$  (base area of  $125 \mu\text{m} \times 125 \mu\text{m}$ ) and fabricated without a pedestal. (b) An SVPC scaled for  $a = 2.0 \mu\text{m}$  (base area of  $40 \mu\text{m} \times 40 \mu\text{m}$ ) and fabricated atop of 110  $\mu\text{m}$  tall pedestal.

#### 2.5. Optical and structural characterization of SPVCs

The optical performance of the SVPCs was characterized using the system shown in Fig. 5. An SVPC was mounted onto a three-axis translation stage and viewed from above with a microscope fitted with a CCD camera. Optical fibers (Thorlabs 1550 BHP, 9  $\mu\text{m}$  core diameter, 10 cm long) were treated on one end with a buffered oxide etch (J.T. Baker 1178-03, 6.5 hours) to reduce the diameter of the cladding to 50  $\mu\text{m}$ . The fibers were mounted on three-axis translation stages and the etched ends were brought to within 5  $\mu\text{m}$  of the SVPC faces. The output of a pulsed Er:YAG laser (Premier Laser,  $\lambda_0 = 2.94 \mu\text{m}$ , 15 mJ/pulses, 10 pulses/sec, and 170  $\mu\text{s}$  pulse duration) was coupled into the “source” fiber, which introduced light onto the entrance face of the SVPC. The remaining “output” fibers collected light emanating from the other faces and directed it to infrared detectors for measurement (Thorlabs PDA20H).

A reference detector measured the relative intensity of each laser pulse. Calibration factors were measured to account for the sensitivity of each detector and the collection efficiency of each fiber. Signals from the output fibers were scaled by the calibration factors and the reference detector output to obtain the normalized intensity as a function of fiber position across a given crystal face. The intensity of light exiting the source fiber was measured by

scanning a second fiber across its output. Neutral density filters were placed before the coupling objective to adjust the source intensity as needed. Fabricating the SVPC atop a 110  $\mu\text{m}$  pedestal and etching back the fiber claddings ensured that the fibers could be scanned across the crystal face without contacting the substrate.

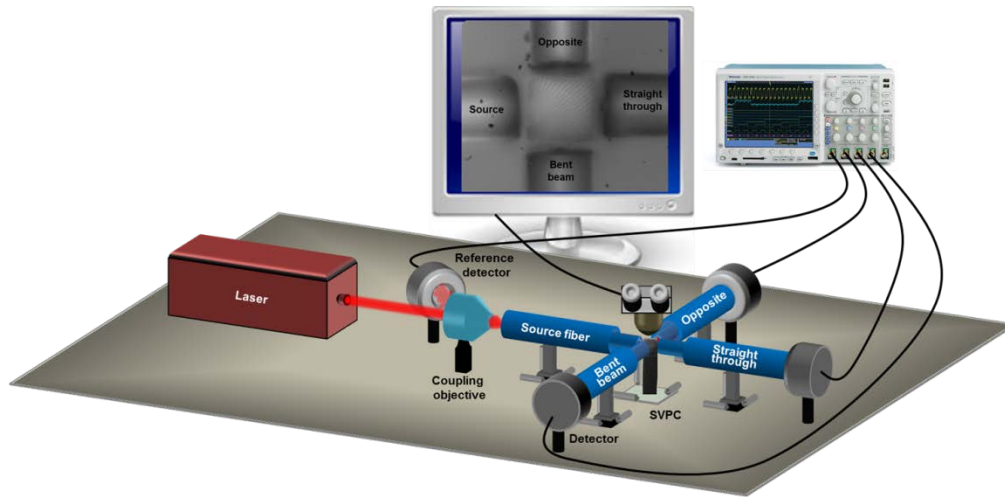


Fig. 5. Apparatus used to characterize optical performance of the SVPCs. The objects are not depicted to scale; the SVPC and optical fibers in particular are drawn large for clarity. The “source fiber” introduces infrared light onto the SVPC. The remaining output fibers collect light emanating from the other SVPC faces and direct it to detectors for measurement. The “bent beam” face is that from which light emerges when directed through the 90° bend, whereas light collected at the “straight through” face is not self-collimated through the turn. The monitor shows a microscope image from an actual measurement.

The light is defined as vertically polarized when the electric field is normal to the surface of the substrate. A wire-grid polarizer (Specac GS57010, BaF<sub>2</sub> substrate) was inserted after the laser to select between vertical and horizontal polarization for certain measurements. Polarization studies of the source showed that the light was not depolarized after traversing the short length of the fibers used. The laser output was elliptically polarized with five times more power in the vertical polarization. Most measurements were performed with the laser output directly coupled into the source fiber, making it predominantly vertically polarized. The wire grid polarizer was used to perform measurements when purely horizontal or vertical polarization was needed. The relative uncertainty in signals measured at the peak of line-scans is  $\pm 15\%$  at the  $3\sigma$ -level and dominated by the shot-to-shot fluctuations in the laser output. Following optical characterization, the SVPCs were imaged by SEM using previously described methods [27].

### 2.6. Simulation of the optical properties of the SPVCs

The full 3D lattice is extremely computationally intensive to simulate. Instead, a 2D model was simulated that was constructed from a single layer of the 3D lattice using an effective index method [Fig. 6]. The effective refractive index at each  $(x,y)$ -position of the 2D lattice was obtained by averaging the refractive index along the corresponding column in the 3D lattice, where the  $n$  and the  $\kappa$  values were taken directly from the ellipsometry measurements. The resulting 2D lattice was modelled using the finite-difference frequency-domain method [32]. In this method, the derivatives in Maxwell’s equations are approximated using central finite-differences. The finite-difference equations are written for every point on the grid and this large set of equations is then cast into matrix form as  $\mathbf{Ax} = \mathbf{b}$ . The field was obtained as  $\mathbf{x} = \mathbf{A}^{-1}\mathbf{b}$ , and used to calculate intensity profiles and bend efficiency through the lattice. A uniaxial perfectly matched layer boundary condition was used to absorb at all four

edges of the grid, with a size of 20 cells at each boundary. The simulation converged at a grid resolution of  $\lambda_0/20$ . The beam source was calculated from a slab waveguide model of the optical fiber used to interrogate the lattice.

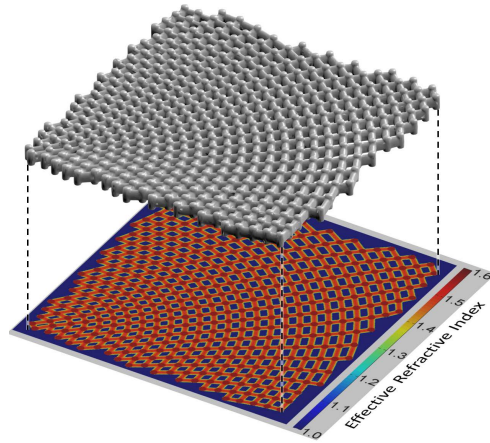


Fig. 6. 2D model used for simulating the SVPCs that was generated from the 3D lattice using the effective index method.

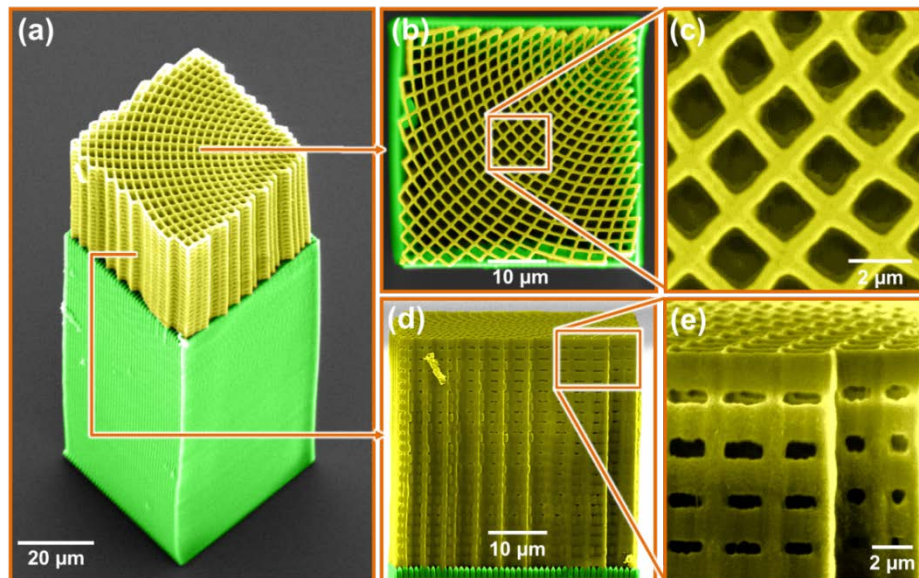


Fig. 7. False-color SEM images of an SVPC with a fill factor of 42%. The structure is viewed (a) from a perspective angle, (b & c) top-down, and (d & e) looking into the side face where the source beam enters during optical characterization.

### 3. Results and discussion

The optical transmission images in Fig. 4 show an SVPC having a large-period ( $a = 5.75 \mu\text{m}$ ) and supported directly by the substrate (no pedestal) and a small-period SVPC ( $a = 2.0 \mu\text{m}$ ) fabricated atop a  $110 \mu\text{m}$  pedestal. The visibility through the SVPCs is naturally poorer for the small-period structure because the unit cells are smaller and the light must first pass through the tall pedestal. Nonetheless, for both structures light passes through the voids formed by adjoining unit cells, confirming that the developing process successfully removes

unpolymerized material from the interior and that adjacent unit cells are aligned, resulting in a well formed, robust, and self-supporting structure.

Figure 7 is a compilation of SEM images showing an SVPC viewed from multiple angles and magnifications. Such images were used to assess the quality of the structure and the form of the unit cells. For all structures, a unit cell at the center of the lattice was selected for measurement of its width (top view), height (center of side view), and the dimensions of the constituent rods. The unit cell dimensions were in turn used to calculate the volumetric fill factor. Figure 8 shows close-up top-views of three other SVPCs fabricated at different fill factors. Across all structures and fill factors, the unit cell widths averaged  $1.92 \mu\text{m}$  (with extreme values within  $\pm 6\%$ ) and the heights averaged  $2.07 \mu\text{m}$  (with extreme values within  $\pm 7\%$ ). These values are very close to the targeted lattice spacing of  $a = 2.0 \mu\text{m}$ . The SEM images confirm that the SVPCs are well formed per the targeted design.

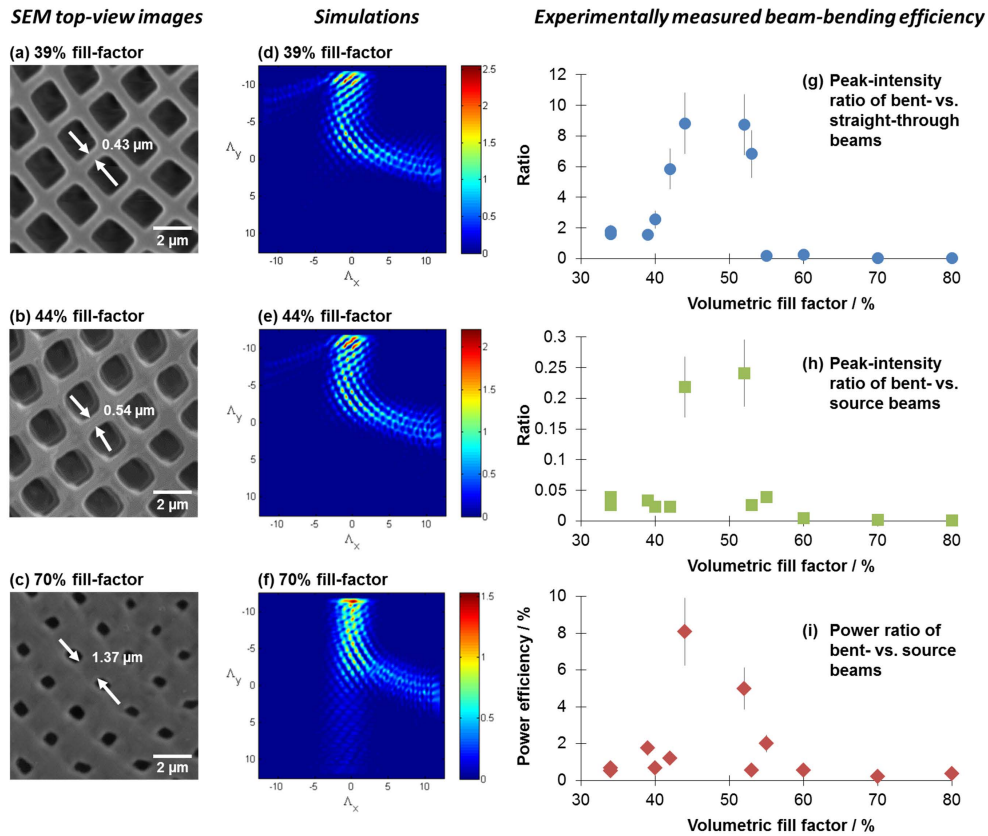


Fig. 8. (a - c) Top-view SEM images of SVPCs having the fill factors indicated and (d - f) simulations of the intensity of vertically-polarized light propagating within them. (g - i) Experimentally measured beam-bending efficiency of SVPCs versus fill factor. The bending efficiency is quantified as (g) the ratio of the peak-intensities for the bent- versus straight-through beams; (h) ratio of peak-intensities for the bent- versus source beams; and (i) the ratio of integrated power in the bent- and source beams.

The ability of SVPCs to flow an optical beam through a tight turn is illustrated in Fig. 9. This image shows the intensity of light incident centered on the input face of an SVPC having a fill factor of 44% and the intensity emanating from the output faces. The peak intensity at the bent-beam face is 8.7 times larger than that exiting the straight-through face, indicating that the lattice directs light strongly through the turn. A small fraction of light also exits at the side opposite of the bent-beam face. This is attributed to scatter from the input face, as

discussed below. There may also be a contribution due to reflection from the bent-beam face, as neither is impedance-matched to the surrounding air. The horizontal intensity profile at the bent-beam output face has a full-width at half-maximum (FWHM) of 12  $\mu\text{m}$ . Vertical line scans had comparable width. In contrast, scanning the fiber opposite to the source with no interposed structure and a separation of 50  $\mu\text{m}$  yielded a trace having a FWHM of 23  $\mu\text{m}$ . The narrower profile of the bent-beam output provides evidence that the beam is directed through the turn by self-collimation within the lattice.

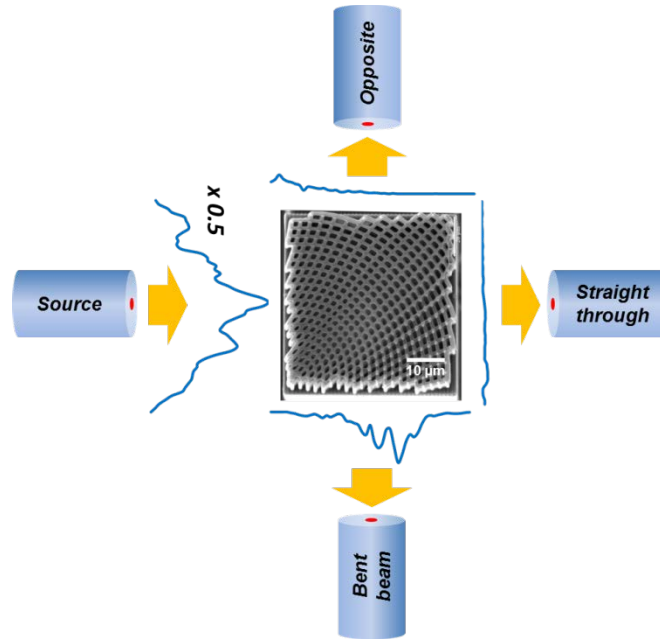


Fig. 9. Horizontal line-scans (blue traces) showing the relative intensity of light at  $\lambda_0 = 2.94 \mu\text{m}$  at the input and output faces of an SVPC (top-view SEM image) with a fill factor of 44%. This SVPC bends light out of the straight-through path toward the bent-beam output face with a peak-to-peak ratio of 8.7.

These particular SVPCs bend beams with a high degree of polarization selectivity due to the asymmetry of the unit cell. Figure 10 shows the relative intensity of light exiting at the bent-beam and straight-through faces when the source is vertically or horizontally polarized. For vertical polarization, the ratio of peak-to-peak intensity at the bent- and straight-through faces is 8:1. However, for horizontal polarization, this ratio is less than 0.1. Vertically polarized light is bent through the turn 25 times more effectively than horizontally polarized light. Additionally, the width of the bent beam is significantly reduced relative to light passing straight through the lattice, which is additional evidence for self-collimation. All of these observations are confirmed by the simulations for the same SVPC, also shown in Fig. 8.

Intensity line-scans, like those in Fig. 9, were measured for SVPCs fabricated with a wide range of fill factors. These data were used to assess the beam-bending efficiency with three metrics: (1) the ratio of the peak-intensities for the bent- and straight- through beams; (2) the ratio of peak intensities for the bent beam and the source beam; and (3) the ratio of relative power in the bent and source beams. The results are presented in Figs. 8(g)-8(i). The overall power of a beam relative to the source was estimated from the linear intensity scans. A given beam was assumed to be circularly symmetric and the integrated total power was obtained by revolving its line scan through 180 degrees.

The peak-to-peak intensity ratio for the bent- and straight-through beams [Fig. 8(g)] exceeds 8:1 for a fill factor of 44% and 52%, indicating that most of the light exiting the lattice was bent through the turn. At higher fill-factors the bending-ratio drops to nearly zero.

Some beam bending occurs for fill factors below 42%, but the efficiency is low, with the bending ratio barely exceeding unity. These data suggest that the beam-bending efficiency is greatest when the fill factor is near 50%. The same conclusion is reached when the beam-bending efficiency is evaluated in terms of the other two metrics [Figs. 8(h) and 8(i)].

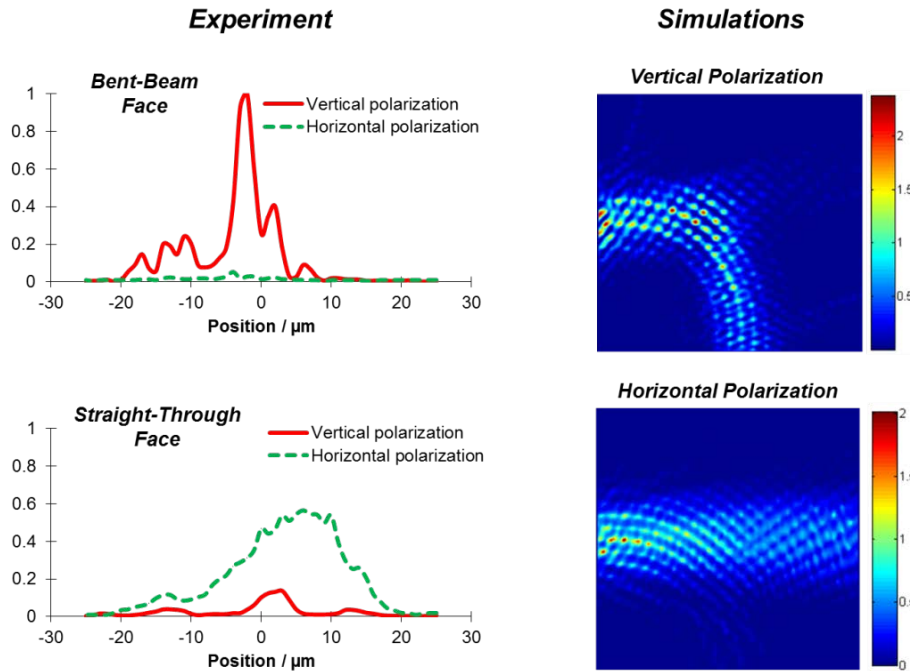


Fig. 10. Polarization dependence of beam bending for a 53% fill factor SVPCs. *(Left)* Experimental line-scans of the intensity for vertically or horizontally polarized light that is bent through the turn or passes straight through the SVPC. *(Right)* Simulations of beam bending in the same SVPC.

For SVPCs having a fill factor near 50%, much more light is bent through the turn than is transmitted straight through the lattice, yet the relative power directed through the bend is only 8%. This is primarily because SU-8 absorbs strongly at  $2.94 \mu\text{m}$ . When the source is incident on the pedestal – which has 100% fill factor and the same path length as the SVPC – the transmission is 25%, which is consistent with the ellipsometry measurements of the absorption coefficient. Reflection losses will be present also for the SVPCs, as well as internal scatter, and scatter of the beam from the rough exit faces. Much more efficient SVPCs could be created by working at wavelengths where the material is more transmissive, using higher-transmission materials, optimizing the fabrication process, and engineering the edges of the lattice to prevent reflections.

The simulations of beam propagation shown in Fig. 8 are in qualitative agreement with all experimental results. It is particularly noteworthy that the beam bending efficiency is predicted to be high for fill factors near 50%. Quantitatively, the simulations predict higher beam-bending efficiency, particularly at low fill factors. The simulations may over-estimate the beam bending efficiency because they are calculated using a 2D lattice. The simulations do predict all key optical performance that is observed experimentally, and even subtle but important features, such as the following. A low-intensity peak is observed experimentally and in simulations of lower-fill-factor SVPCs at the *opposite* face, close to the source [e.g., see Figs. 7 and 9]. This suggests that the lattices could be better designed and fabricated to optimize insertion loss at the entrance and exit faces.

Comparing SVPCs to other approaches for beam bending is challenging because the performance of a given device depends on multiple parameters that may be chosen differently to satisfy specific design requirements. Nonetheless, it is helpful to make a comparison using existing reports, making note of differences in material, fabrication complexity, and functional advantages and disadvantages. Table 1 lists  $R_{\text{bend}}/\lambda_0$  and the refractive index contrast  $\Delta n$  for beam-bending devices of multiple architectures. For each of these devices, larger  $\Delta n$  yields stronger interaction with the optical field and the potential for tighter bending. On this basis, the product  $(R_{\text{bend}}/\lambda_0) \times \Delta n$  is offered as a performance metric and calculated for each device, where a lower value corresponds to better performance.

**Table 1. Comparison of approaches for bending a beam through a 90 degree turn or greater. Each entry includes the bend radius  $R_{\text{bend}}$  divided by the operating wavelength  $\lambda_0$  and the refractive index contrast  $\Delta n$  of the materials used to create the device. The performance metric  $(R_{\text{bend}}/\lambda_0) \times \Delta n$  is calculated to aid comparison between approaches.**

Approach	$R_{\text{bend}} / \lambda_0$	Index contrast ( $\Delta n$ )	Performance metric ( $R_{\text{bend}}/\lambda_0) \times \Delta n$	Method
SVPC for IR wavelengths, this work	6.4	0.57	3.7	Exp. & Calc.
SVPC for microwaves [4]	6.4	0.56	3.6	Exp. & Calc.
High- $\Delta n$ square waveguide, this work	12.9	0.57	7.4	Calculation
Low- $\Delta n$ square waveguide [34]	3032	0.009	27.3	Calculation <sup>1</sup>
Graded-period photonic crystal [11]	2.45	2.00	4.9	Calculation
Graded refractive index medium [38]	8.0	2.13	17.0	Calculation
Parallelogram-lattice photonic crystal [39]	7.57	2.46	18.6	Calculation
Si graded-fill-factor photonic crystal [10]	3.75	1.95	7.3	Calculation
Si-on-insulator graded fill-factor photonic crystal [6]	20.0	2.46	49.2	Exp. & Calc.
Cu graded-period photonic crystal for microwaves [9]	3.5	NA	NA	Exp. & Calc.
Plasmonic waveguide [33]	1.29	~0.5	0.65	Exp. & Calc. <sup>2</sup>

1. Using the authors' recommended parameters for a waveguide at  $\lambda_0 = 1550$  nm, the cross-section is  $5 \mu\text{m} \times 5 \mu\text{m}$ ,  $R_{\text{bend}} = 4.7 \mu\text{m}$ , and the resulting loss is 8.5 dB.

2. Gold nanowire waveguide, 70 nm wide, with  $R_{\text{bend}} = 2 \mu\text{m}$ ,  $\lambda_0 = 1550$  nm, amplitude-transmission = 0.5, and per the authors,  $n(\text{Au}) \sim n(\text{BK7 glass}) = 1.5$ .

In terms of the performance metric, SVPCs are superior to all beam bending devices listed in Table 1, other than the 70 nm wide plasmonic nanowire waveguide [33]. Although the plasmonic waveguide offers the smallest  $R_{\text{bend}}$ , the loss is substantial, with the transmission *amplitude* reaching only 3 dB. Wang *et al.* [34] optimized  $R_{\text{bend}}$  versus loss for low- $\Delta n$  waveguides with square cross-section and the loss reaches 8.5 dB for a bend radius as high as  $R_{\text{bend}} = 4.7 \mu\text{m}$ . To evaluate the bending efficiency of high- $\Delta n$  waveguides, we used the COMSOL simulation environment to calculate the eigenmodes of a circular air-clad waveguide at  $\lambda_0 = 2.94 \mu\text{m}$  with a  $9 \mu\text{m} \times 9 \mu\text{m}$  square cross-section and the same  $\Delta n$  as that of the SVPCs. We find that the fundamental mode is lost for  $R_{\text{bend}} < 38 \mu\text{m}$ , which corresponds to  $(R_{\text{bend}}/\lambda_0) \times \Delta n = 7.4$ . Higher order modes are lost at larger values of  $R_{\text{bend}}$ .

Thus, the SVPCs enable beam bending within less than half the radius, or one quarter of the area, required by conventional waveguides, and without loss of higher order modes.

The other approaches listed in Table 1 involve using photonic crystals or other periodic media having graded period, fill factor, or effective refractive index. Graded-period photonic crystals come closest to the performance metric obtained for SVPCs, although we note that this example and most others are not experimentally demonstrated. Two employ high-index media (e.g., silicon), and even then they do not perform as well as SVPCs. The challenges associated with fabricating these alternative devices are substantial, particularly where graded fill-factor is required, and only 2D structures are accessible. It is likely, however, that many photonic architectures will require 3D beam bending, in which case SVPCs are far better suited and they provide better performance, with DLW providing a means to create them.

The experimental work reported here considers an SVPC that is  $22 \times 22$  unit cells. Theoretical work by several of us [4] qualitatively estimates the minimum bend radius of one specific lattice. In this work, self-collimation around a bend is still apparent for SVPCs as small as  $12 \times 12$  unit cells ( $R_{\text{bend}} = 3.1\lambda_0$ ), although these suffer greater loss due to being near the threshold of minimum bend radius.

DLW could be used to create SVPCs that bend beams at shorter wavelengths and with much larger beam sizes. Multi-beam schemes for DLW have been used to create features with a lateral resolution as small as 55 nm [35] and an axial resolution of 40 nm [36]. Thus, DLW could be used to create complex integrated photonic circuits operating in the telecommunication window. The method has also been used to create microstructures hundreds of microns in size [37], so SVPCs could also be created for guiding structured sub-millimeter beams for related imaging applications.

Using SVPCs created by DLW, other parameters such as fill factor and lattice spacing can be easily adjusted in addition to unit cell orientation to achieve even more degrees of beam control. This is clear from the present example, where the beam is directed through a turn with selectivity over the polarization. But the potential of SVPCs is far greater. Other lattice parameters could be adjusted to control not only power flow but also phase, which is not controlled in the present example. Phase could be used to generate a beam that focuses upon exiting this SVPC. This provides even greater functionality, including a means to couple outputs to conventional waveguides or free-space components, with minimal insertion loss. Lastly, the SVPC demonstrated here can be made polarization insensitive by fabricating a symmetric unit cell.

#### 4. Conclusion

This work demonstrates that 3D SVPCs can steer a light beam through a turn with radius as small as  $6.4\lambda_0$  while also providing control over polarization. The SVPCs were designed, fabricated, and optically characterized, and their performance was compared to electromagnetic simulations. The experimental characterization shows that these particular SVPCs provide effective beam control for vertically polarized light when the fill factor is near 50%. Numerical simulations confirm this behavior and provide insight into how performance can be significantly improved.

Unlike dielectric waveguides that function based on total internal reflection, SVPCs can control the direction of beams that have complex irradiance profiles, without bias against higher-order modes. This provides an important new solution for integrated photonics applications where a means is sought for controlling beams that have complex profiles [40]. Additionally, there is no restriction on the size of the beam that can be steered. So in principle 3D SVPCs could be designed and fabricated for directing macroscopic beams and imaging at visible and infrared wavelengths. Larger-period SVPCs could potentially be used to control THz waves [41].

## Appendix

**Table 2. Values of ordinary refractive index ( $n$ ) and extinction coefficient ( $\kappa$ ) versus vacuum wavelength ( $\lambda_0$ ) obtained from ellipsometry measurements of a cross-linked 1.6  $\mu\text{m}$  thick SU-8 film using VASE and IR-VASE instruments (W. A. Woollam), as plotted in Fig. 2.**

VASE Measurements			VASE Measurements			VASE Measurements		
$\lambda_0 / \mu\text{m}$	$n$	$\kappa$	$\lambda_0 / \mu\text{m}$	$n$	$\kappa$	$\lambda_0 / \mu\text{m}$	$n$	$\kappa$
0.500	1.6094	0	0.970	1.5812	0	1.510	1.5754	0
0.510	1.6078	0	0.980	1.5810	0	1.520	1.5754	0
0.520	1.6064	0	0.990	1.5808	0	1.530	1.5753	0
0.530	1.6050	0	1.000	1.5806	0	1.540	1.5753	0
0.540	1.6038	0	1.010	1.5804	0	1.550	1.5752	0
0.550	1.6026	0	1.020	1.5802	0	1.560	1.5752	0
0.560	1.6014	0	1.030	1.5801	0	1.570	1.5751	0
0.570	1.6003	0	1.040	1.5799	0	1.580	1.5751	0
0.580	1.5993	0	1.050	1.5797	0	1.590	1.5750	0
0.590	1.5984	0	1.060	1.5796	0	1.600	1.5750	0
0.600	1.5974	0	1.070	1.5794	0	1.610	1.5749	0
0.610	1.5966	0	1.080	1.5793	0	1.620	1.5749	0
0.620	1.5957	0	1.090	1.5791	0	1.630	1.5748	0
0.630	1.5950	0	1.100	1.5790	0	1.640	1.5748	0
0.640	1.5942	0	1.110	1.5789	0	1.650	1.5748	0
0.650	1.5935	0	1.120	1.5787	0	1.660	1.5747	0
0.660	1.5928	0	1.130	1.5786	0	1.670	1.5747	0
0.670	1.5922	0	1.140	1.5785	0	1.680	1.5746	0
0.680	1.5915	0	1.150	1.5783	0	1.690	1.5746	0
0.690	1.5910	0	1.160	1.5782	0	1.700	1.5746	0
0.700	1.5904	0	1.170	1.5781	0	1.710	1.5745	0
0.710	1.5898	0	1.180	1.5780	0	1.720	1.5745	0
0.720	1.5893	0	1.190	1.5779	0	1.730	1.5745	0
0.730	1.5888	0	1.200	1.5778	0	1.740	1.5744	0
0.740	1.5883	0	1.210	1.5777	0	1.750	1.5744	0
0.750	1.5879	0	1.220	1.5776	0	1.760	1.5743	0
0.760	1.5875	0	1.230	1.5775	0	1.770	1.5743	0
0.770	1.5870	0	1.240	1.5774	0	1.780	1.5743	0
0.780	1.5866	0	1.250	1.5773	0	1.790	1.5743	0
0.790	1.5862	0	1.260	1.5772	0	1.800	1.5742	0
0.800	1.5859	0	1.270	1.5771	0	1.810	1.5742	0
0.810	1.5855	0	1.280	1.5770	0	1.820	1.5742	0
0.820	1.5852	0	1.290	1.5769	0	1.830	1.5741	0
0.830	1.5848	0	1.300	1.5768	0	1.840	1.5741	0
0.840	1.5845	0	1.310	1.5767	0	1.850	1.5741	0
0.850	1.5842	0	1.320	1.5767	0	1.860	1.5740	0
0.860	1.5839	0	1.330	1.5766	0	1.870	1.5740	0
0.870	1.5836	0	1.340	1.5765	0	1.880	1.5740	0
0.880	1.5833	0	1.350	1.5764	0	1.890	1.5740	0
0.890	1.5830	0	1.430	1.5759	0	1.900	1.5739	0
0.900	1.5828	0	1.440	1.5758	0	1.910	1.5739	0
0.910	1.5825	0	1.450	1.5758	0	1.920	1.5739	0
0.920	1.5823	0	1.460	1.5757	0	1.930	1.5739	0
0.930	1.5821	0	1.470	1.5756	0	1.940	1.5738	0
0.940	1.5818	0	1.480	1.5756	0	1.950	1.5738	0
0.950	1.5816	0	1.490	1.5755	0	1.960	1.5738	0
0.960	1.5814	0	1.500	1.5755	0	1.970	1.5738	0

VASE Measurements			IR-VASE Measurements			IR-VASE Measurements		
$\lambda_0 / \mu\text{m}$	$n$	$\kappa$	$\lambda_0 / \mu\text{m}$	$n$	$\kappa$	$\lambda_0 / \mu\text{m}$	$n$	$\kappa$
1.980	1.5737	0	2.0641	1.5758	$3.70 \times 10^{-5}$	2.5821	1.5715	$8.10 \times 10^{-4}$
1.990	1.5737	0	2.0773	1.5758	$3.93 \times 10^{-5}$	2.5925	1.5713	$8.45 \times 10^{-4}$
2.000	1.5737	0	2.0840	1.5757	$4.41 \times 10^{-5}$	2.6029	1.5712	$8.82 \times 10^{-4}$
			2.0975	1.5757	$4.68 \times 10^{-5}$	2.6134	1.5710	$9.21 \times 10^{-4}$
			2.1043	1.5756	$5.25 \times 10^{-5}$	2.6239	1.5708	$9.65 \times 10^{-4}$
			2.1180	1.5756	$5.55 \times 10^{-5}$	2.6346 10-	1.5706	$1.01 \times 10^{-3}$
			2.1250	1.5755	$6.22 \times 10^{-5}$	2.6454	1.5704	$1.07 \times 10^{-3}$
			2.1390	1.5754	$6.58 \times 10^{-5}$	2.6562	1.5702	$1.14 \times 10^{-3}$
			2.1461	1.5754	$6.96 \times 10^{-5}$	2.6671	1.5699	$1.23 \times 10^{-3}$
			2.1532	1.5753	$7.77 \times 10^{-5}$	2.6782	1.5696	$1.34 \times 10^{-3}$
			2.1676	1.5752	$8.21 \times 10^{-5}$	2.6893	1.5693	$1.49 \times 10^{-3}$
			2.1749	1.5752	$9.16 \times 10^{-5}$	2.7005	1.5690	$1.67 \times 10^{-3}$
			2.1896	1.5751	$9.66 \times 10^{-5}$	2.7118	1.5687	$1.91 \times 10^{-3}$
			2.1970	1.5751	$1.02 \times 10^{-4}$	2.7232	1.5683	$2.22 \times 10^{-3}$
			2.2045	1.5750	$1.13 \times 10^{-4}$	2.7347	1.5680	$2.60 \times 10^{-3}$
			2.2196	1.5749	$1.20 \times 10^{-4}$	2.7462	1.5677	$3.05 \times 10^{-3}$
			2.2272	1.5748	$1.26 \times 10^{-4}$	2.7579	1.5675	$3.59 \times 10^{-3}$
			2.2349	1.5748	$1.33 \times 10^{-4}$	2.7697	1.5673	$4.19 \times 10^{-3}$
			2.2426	1.5747	$1.47 \times 10^{-4}$	2.7816	1.5672	$4.86 \times 10^{-3}$
			2.2582	1.5746	$1.55 \times 10^{-4}$	2.7936	1.5673	$5.55 \times 10^{-3}$
			2.2661	1.5746	$1.63 \times 10^{-4}$	2.8057	1.5675	$6.24 \times 10^{-3}$
			2.2741	1.5745	$1.72 \times 10^{-4}$	2.8179	1.5678	$6.89 \times 10^{-3}$
			2.2821	1.5744	$1.90 \times 10^{-4}$	2.8302	1.5683	$7.47 \times 10^{-3}$
			2.2983	1.5743	$2.00 \times 10^{-4}$	2.8426	1.5689	$7.93 \times 10^{-3}$
			2.3065	1.5743	$2.10 \times 10^{-4}$	2.8551	1.5695	$8.24 \times 10^{-3}$
			2.3147	1.5742	$2.20 \times 10^{-4}$	2.8678	1.5702	$8.38 \times 10^{-3}$
			2.3230	1.5741	$2.43 \times 10^{-4}$	2.8805	1.5709	$8.36 \times 10^{-3}$
			2.3398	1.5740	$2.55 \times 10^{-4}$	2.8934	1.5716	$8.17 \times 10^{-3}$
			2.3482	1.5739	$2.68 \times 10^{-4}$	2.9063	1.5721	$7.84 \times 10^{-3}$
			2.3568	1.5739	$2.81 \times 10^{-4}$	2.9194	1.5726	$7.39 \times 10^{-3}$
			2.3654	1.5738	$2.94 \times 10^{-4}$	2.9326	1.5729	$6.87 \times 10^{-3}$
			2.3740	1.5737	$3.09 \times 10^{-4}$	2.9460	1.5730	$6.31 \times 10^{-3}$
			2.3828	1.5736	$3.23 \times 10^{-4}$	2.9594	1.5730	$5.76 \times 10^{-3}$
			2.3916	1.5735	$3.55 \times 10^{-4}$	2.9730	1.5729	$5.23 \times 10^{-3}$
			2.4093	1.5734	$3.72 \times 10^{-4}$	2.9867	1.5726	$4.77 \times 10^{-3}$
			2.4183	1.5733	$3.89 \times 10^{-4}$	3.0005	1.5723	$4.38 \times 10^{-3}$
			2.4274	1.5732	$4.07 \times 10^{-4}$	3.0145	1.5719	$4.06 \times 10^{-3}$
			2.4365	1.5731	$4.26 \times 10^{-4}$	3.0286	1.5715	$3.82 \times 10^{-3}$
			2.4457	1.5730	$4.45 \times 10^{-4}$	3.0428	1.5710	$3.66 \times 10^{-3}$
			2.4550	1.5730	$4.66 \times 10^{-4}$	3.0571	1.5705	$3.56 \times 10^{-3}$
			2.4643	1.5729	$4.87 \times 10^{-4}$	3.0716	1.5700	$3.51 \times 10^{-3}$
			2.4737	1.5728	$5.09 \times 10^{-4}$	3.0863	1.5695	$3.51 \times 10^{-3}$
			2.4832	1.5727	$5.31 \times 10^{-4}$	3.1010	1.5690	$3.54 \times 10^{-3}$
			2.4927	1.5726	$5.55 \times 10^{-4}$	3.1159	1.5685	$3.59 \times 10^{-3}$
			2.5024	1.5725	$5.79 \times 10^{-4}$	3.1310	1.5680	$3.66 \times 10^{-3}$
			2.5121	1.5724	$6.05 \times 10^{-4}$	3.1462	1.5674	$3.76 \times 10^{-3}$
			2.5218	1.5722	$6.31 \times 10^{-4}$	3.1615	1.5667	$3.88 \times 10^{-3}$
			2.5317	1.5721	$6.58 \times 10^{-4}$	3.1770	1.5660	$4.04 \times 10^{-3}$
			2.5416	1.5720	$6.86 \times 10^{-4}$	3.1927	1.5651	$4.27 \times 10^{-3}$
			2.5516	1.5719	$7.16 \times 10^{-4}$	3.2085	1.5640	$4.65 \times 10^{-3}$
			2.5617	1.5718	$7.46 \times 10^{-4}$	3.2244	1.5628	$5.26 \times 10^{-3}$
			2.5719	1.5716	$7.78 \times 10^{-4}$	3.2406	1.5614	$6.24 \times 10^{-3}$

IR-VASE Measurements			IR-VASE Measurements			IR-VASE Measurements		
$\lambda_0 / \mu\text{m}$	$n$	$\kappa$	$\lambda_0 / \mu\text{m}$	$n$	$\kappa$	$\lambda_0 / \mu\text{m}$	$n$	$\kappa$
3.2569	1.5600	$7.72 \times 10^{-3}$	4.2085	1.5707	$1.02 \times 10^{-2}$	5.9460	1.5454	$1.50 \times 10^{-2}$
3.2733	1.5587	$9.83 \times 10^{-3}$	4.2360	1.5707	$1.03 \times 10^{-2}$	6.0010	1.5410	$1.97 \times 10^{-2}$
3.2899	1.5578	$1.26 \times 10^{-2}$	4.2639	1.5706	$1.04 \times 10^{-2}$	6.0571	1.5403	$2.74 \times 10^{-2}$
3.3067	1.5577	$1.60 \times 10^{-2}$	4.2921	1.5705	$1.05 \times 10^{-2}$	6.1143	1.5456	$3.27 \times 10^{-2}$
3.3237	1.5587	$1.96 \times 10^{-2}$	4.3208	1.5704	$1.06 \times 10^{-2}$	6.1725	1.5517	$3.06 \times 10^{-2}$
3.3408	1.5610	$2.31 \times 10^{-2}$	4.3498	1.5703	$1.08 \times 10^{-2}$	6.2318	1.5513	$2.37 \times 10^{-2}$
3.3581	1.5644	$2.58 \times 10^{-2}$	4.3791	1.5702	$1.09 \times 10^{-2}$	6.2924	1.5437	$1.85 \times 10^{-2}$
3.3756	1.5686	$2.74 \times 10^{-2}$	4.4089	1.5701	$1.10 \times 10^{-2}$	6.3540	1.5311	$1.75 \times 10^{-2}$
3.3933	1.5732	$2.75 \times 10^{-2}$	4.4391	1.5700	$1.11 \times 10^{-2}$	6.4170	1.5099	$2.42 \times 10^{-2}$
3.4111	1.5774	$2.61 \times 10^{-2}$	4.4698	1.5699	$1.12 \times 10^{-2}$	6.4811	1.4892	$6.38 \times 10^{-2}$
3.4292	1.5807	$2.36 \times 10^{-2}$	4.5008	1.5698	$1.13 \times 10^{-2}$	6.5466	1.5288	$1.09 \times 10^{-1}$
3.4474	1.5830	$2.04 \times 10^{-2}$	4.5323	1.5697	$1.14 \times 10^{-2}$	6.6134	1.5682	$9.47 \times 10^{-2}$
3.4658	1.5839	$1.70 \times 10^{-2}$	4.5642	1.5696	$1.15 \times 10^{-2}$	6.6816	1.5809	$8.22 \times 10^{-2}$
3.4845	1.5839	$1.39 \times 10^{-2}$	4.5965	1.5694	$1.16 \times 10^{-2}$	6.7512	1.5929	$6.63 \times 10^{-2}$
3.5033	1.5831	$1.14 \times 10^{-2}$	4.6294	1.5693	$1.17 \times 10^{-2}$	6.8223	1.5914	$4.71 \times 10^{-2}$
3.5224	1.5818	$9.52 \times 10^{-3}$	4.6627	1.5692	$1.17 \times 10^{-2}$	6.8948	1.5812	$3.70 \times 10^{-2}$
3.5416	1.5805	$8.27 \times 10^{-3}$	4.6965	1.5690	$1.18 \times 10^{-2}$	6.9690	1.5719	$3.51 \times 10^{-2}$
3.5611	1.5792	$7.53 \times 10^{-3}$	4.7307	1.5689	$1.19 \times 10^{-2}$	7.0447	1.5658	$3.60 \times 10^{-2}$
3.5807	1.5780	$7.15 \times 10^{-3}$	4.7655	1.5687	$1.20 \times 10^{-2}$	7.1221	1.5615	$3.72 \times 10^{-2}$
3.6006	1.5770	$7.01 \times 10^{-3}$	4.8008	1.5685	$1.21 \times 10^{-2}$	7.2012	1.5573	$3.81 \times 10^{-2}$
3.6207	1.5762	$7.01 \times 10^{-3}$	4.8367	1.5684	$1.21 \times 10^{-2}$	7.2822	1.5522	$3.91 \times 10^{-2}$
3.6411	1.5755	$7.08 \times 10^{-3}$	4.8730	1.5682	$1.22 \times 10^{-2}$	7.3649	1.5455	$4.13 \times 10^{-2}$
3.6617	1.5750	$7.19 \times 10^{-3}$	4.9100	1.5680	$1.23 \times 10^{-2}$	7.4496	1.5376	$4.61 \times 10^{-2}$
3.6825	1.5745	$7.31 \times 10^{-3}$	4.9474	1.5677	$1.23 \times 10^{-2}$	7.5362	1.5295	$5.42 \times 10^{-2}$
3.7035	1.5742	$7.44 \times 10^{-3}$	4.9855	1.5675	$1.24 \times 10^{-2}$	7.6249	1.5213	$6.44 \times 10^{-2}$
3.7248	1.5738	$7.58 \times 10^{-3}$	5.0241	1.5672	$1.24 \times 10^{-2}$	7.7156	1.5069	$8.01 \times 10^{-2}$
3.7463	1.5735	$7.71 \times 10^{-3}$	5.0634	1.5669	$1.25 \times 10^{-2}$	7.8086	1.4922	$1.26 \times 10^{-1}$
3.7681	1.5733	$7.84 \times 10^{-3}$	5.1033	1.5666	$1.26 \times 10^{-2}$	7.9038	1.5414	$1.94 \times 10^{-1}$
3.7901	1.5730	$7.98 \times 10^{-3}$	5.1438	1.5663	$1.26 \times 10^{-2}$	8.0014	1.6337	$1.78 \times 10^{-1}$
3.8124	1.5728	$8.11 \times 10^{-3}$	5.1849	1.5659	$1.26 \times 10^{-2}$	8.1014	1.6546	$1.11 \times 10^{-1}$
3.8350	1.5726	$8.25 \times 10^{-3}$	5.2267	1.5655	$1.27 \times 10^{-2}$	8.2040	1.6319	$8.31 \times 10^{-2}$
3.8578	1.5724	$8.38 \times 10^{-3}$	5.2692	1.5651	$1.27 \times 10^{-2}$	8.3092	1.6209	$7.98 \times 10^{-2}$
3.8809	1.5723	$8.52 \times 10^{-3}$	5.3124	1.5646	$1.28 \times 10^{-2}$	8.4171	1.6155	$7.47 \times 10^{-2}$
3.9043	1.5721	$8.65 \times 10^{-3}$	5.3563	1.5641	$1.28 \times 10^{-2}$	8.5278	1.6030	$7.39 \times 10^{-2}$
3.9280	1.5720	$8.78 \times 10^{-3}$	5.4009	1.5635	$1.28 \times 10^{-2}$	8.6415	1.5935	$9.06 \times 10^{-2}$
3.9519	1.5718	$8.91 \times 10^{-3}$	5.4463	1.5629	$1.28 \times 10^{-2}$	8.7583	1.6088	$1.13 \times 10^{-1}$
3.9762	1.5717	$9.04 \times 10^{-3}$	5.4925	1.5621	$1.29 \times 10^{-2}$	8.8782	1.6386	$1.09 \times 10^{-1}$
4.0007	1.5716	$9.17 \times 10^{-3}$	5.5394	1.5613	$1.29 \times 10^{-2}$	9.0015	1.6482	$8.51 \times 10^{-2}$
4.0256	1.5715	$9.30 \times 10^{-3}$	5.5872	1.5604	$1.29 \times 10^{-2}$	9.1283	1.6343	$7.34 \times 10^{-2}$
4.0507	1.5713	$9.43 \times 10^{-3}$	5.6358	1.5594	$1.29 \times 10^{-2}$	9.2587	1.6241	$8.53 \times 10^{-2}$
4.0762	1.5712	$9.56 \times 10^{-3}$	5.6852	1.5582	$1.29 \times 10^{-2}$	9.3929	1.6349	$1.03 \times 10^{-1}$
4.1020	1.5711	$9.68 \times 10^{-3}$	5.7355	1.5567	$1.29 \times 10^{-2}$	9.5311	1.6610	$1.08 \times 10^{-1}$
4.1281	1.5710	$9.81 \times 10^{-3}$	5.7867	1.5550	$1.30 \times 10^{-2}$	9.6733	1.6865	$9.39 \times 10^{-2}$
4.1546	1.5709	$9.93 \times 10^{-3}$	5.8389	1.5528	$1.30 \times 10^{-2}$	9.8199	1.6997	$6.86 \times 10^{-2}$
4.1814	1.5708	$1.01 \times 10^{-2}$	5.8920	1.5497	$1.34 \times 10^{-2}$	9.9710	1.7013	$5.84 \times 10^{-2}$

## Acknowledgments

This work was supported by NSF CAREER Awards DMR/CHE-0748712 and ECCS-1150672 and by NSF grants number 128208, 1204993, and 1068050. Research at UTEP was supported in part by DARPA through a 2011 Young Faculty Award. The authors thank the referees for their many helpful comments.